LETTER

Hydride-Based Interlayer for Solid-State Anode-Free Battery

Yonglin Huang, Yuxuan Zhang, Ruixin Wu, Bowen Shao, Ruihao Deng, Ratnottam Das, and Fudong Han*

Read Online

ACCESS | Metrics & More | Article Recommendations | SI Supporting Information

ABSTRACT: Solid-state batteries (SSBs) are considered a promising approach to realizing an anode-free concept with high energy densities. However, the initial Coulombic efficiency (ICE) has remained insufficient for anode-free batteries using sulfide-based solid electrolytes (SEs). Herein, we incorporated a hydride-based interlayer, $3LiBH_4$-LiI (LBHI), between a typical sulfide SE, Li_6PS_5Cl, and the Cu current collector. By investigating the Li plating and stripping behaviors and the (electro)chemical stability between SEs and plated Li, we demonstrated that LBHI can effectively improve interfacial stability, leading to an ICE exceeding 94% in anode-free half cells. This interlayer also improves Coulombic efficiencies and specific capacities in anode-free full cells. Furthermore, the utilization of LBHI enables one to study Li plating behaviors without interference from interfacial (electro)chemical instabilities. The analysis of stack pressure evolution during electrochemical cycling reveals that soft shorting in SSBs arises from both dendrite formation and deformation, offering insights into further optimizing solid-state anode-free batteries.
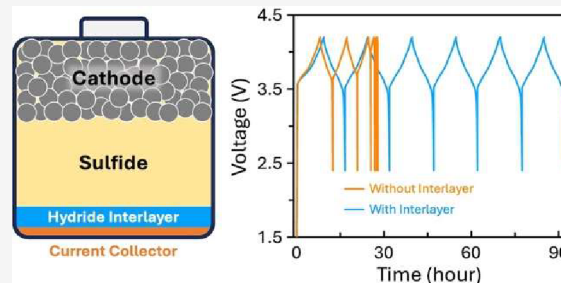
Anode-free batteries have been considered promising to achieve higher energy densities. As anode-free batteries operate without lithium excess, the Coulombic efficiency (CE) determines their cycling performance. As the relation between the CE and the residual lithium reservoir follows a power law, even a slight increase in CE can improve the cycle life. Extensive efforts have been devoted to developing anode-free batteries using liquid electrolytes, including liquid electrolyte formulation,[1,2] current collector design,[3,4] charge/discharge protocols design,[5,6] and interlayer development.[7] However, fabricating long-cycle-life anode-free cells based on liquid electrolytes remains challenging mainly due to the intrinsic instability between liquid electrolytes and Li metal. This instability leads to irreversible consumption of limited lithium due to solid electrolyte interphase (SEI) formation. Moreover, the SEI cannot withstand repeated Li plating and stripping, resulting in its continuous reformation. Li plating in liquid electrolytes may generate high-surface-area mossy or dendritic morphologies and thus exacerbate SEI formation. The dissolution of Li dendrites at their roots can also cause detachment of Li from the anode, forming inactive "dead Li".

Recent studies have highlighted the potential of using inorganic solid electrolytes (SEs) to achieve high-performance anode-free batteries.[8] SEs are not as infiltrative as liquids, reducing the dynamic SEI formation. The surface area of Li

dendrites formed in dense, rigid SEs is expected to be much smaller than those formed in liquid electrolytes. Moreover, the use of SEs reduces the formation of "dead Li". These factors collectively lead to a notable improvement in CEs in solid-state anode-free batteries. The first anode-free cell was constructed over two decades ago using lithium phosphorus oxynitride (LiPON) as SE, and it is still one of the highest-performing anode-free cells to date.[9] This cell, composed of deposited $LiCoO_2$, LiPON, Cu, and a backing layer, can exhibit a CE of >99.98% and cycle over 1000 times at 1 mA/cm².[10] These results have inspired researchers to extend this success by using novel, highly conductive SEs, such as lithium garnet oxide $Li_7La_3Zr_2O_{12}$ (LLZO) and sulfide-based lithium argyrodite Li_6PS_5Cl (LPSCl), to further improve energy density.[11] LLZO-based anode-free cells (Cu|LLZO|Li) reported by Sakamoto et al. can achieve a CE of >95%. They also studied the electro-chemo-mechanics of Li plating and stripping.[12,13] However, realizing a high-energy-density LLZO-based anode-free battery remains a long-term goal due to difficulties in fabricating and
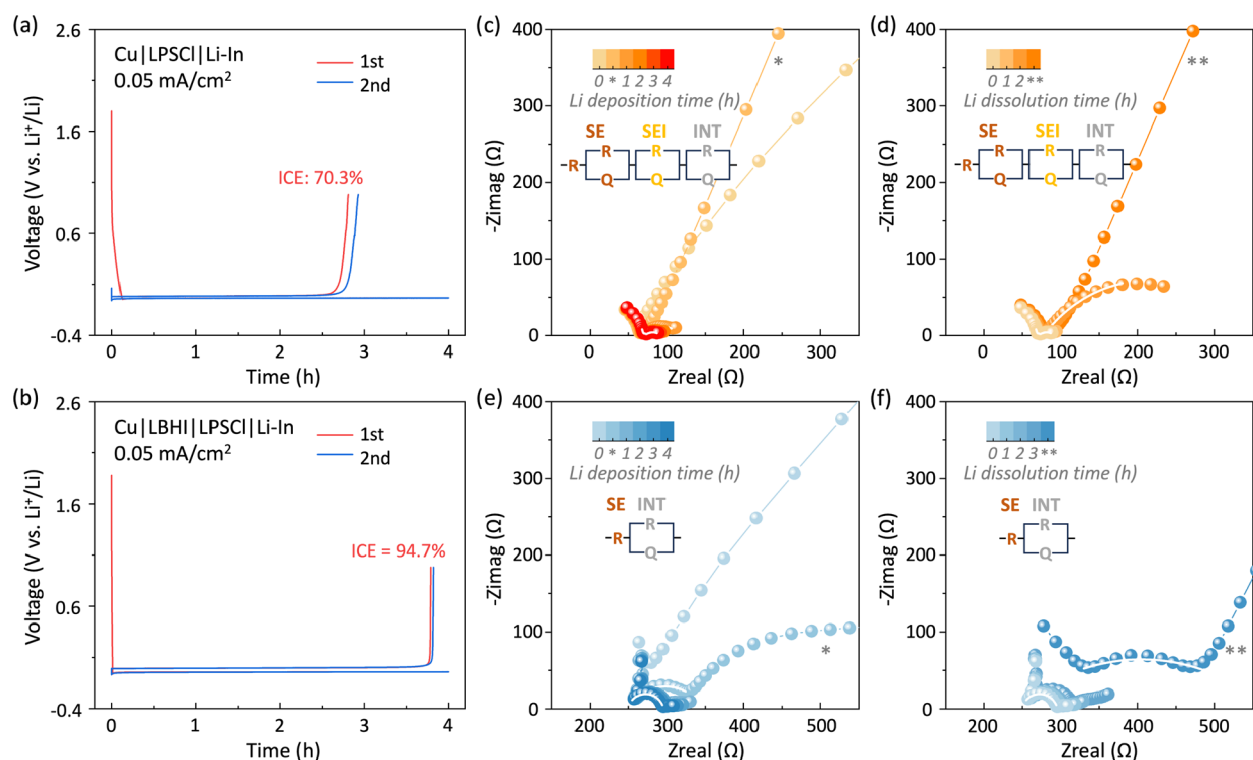
Figure 1. Voltage profiles and ICEs of (a) Cu|LPSCl|Li−In and (b) Cu|LBHI|LPSCl|Li−In half cells. The cells were tested at 0.05 mA/cm² with no stack pressure at room temperature. Nyquist plots of Cu|LPSCl|Li−In and Cu|LBHI|LPSCl|Li−In cells (with 15 MPa stack pressure) during Li plating (c, e) and Li stripping (d, f) during the first cycle. The insets show the equivalent circuits used to fit the impedance. The symbols * and ** represent the moments when the highest overpotential was achieved at the beginning of Li plating and when the cutoff voltage was reached during Li stripping, respectively.

integrating thin LLZO membranes[14] and mitigating interfacial resistances between LLZO and mainstream cathodes.[15,16]

On the other hand, sulfide-based SEs exhibit favorable mechanical and transport properties, making them suitable for practical solid-state batteries (SSBs).[17] Anode-free cells using sulfide-based SEs, particularly LPSCl, have been demonstrated by several research groups.[18−21] However, the initial Coulombic efficiency (ICE) has been limited to around 80%[20,21] due to the limited cathodic stability of LPSCl. Previous studies have revealed that the onset potential for the reduction of LPSCl is 1.7 V vs Li⁺/Li.[22−24] This reduction process can produce a heterogeneous composite of binary compounds, including Li_2S, Li_3P, and LiCl, at the interface. The interphase thickness measured by ToF-SIMS is around 250 nm.[25] Moreover, the thickness of this interphase increases over time based on the diffusion-controlled mechanism.[26,27] Although the original thickness of SEI and its growth rate are limited, which explains why Li|LPSCl|Li cells with sufficient Li can cycle for hundreds of hours at lower currents,[28,29] it is believed that the extent of side reactions is still too high to achieve long-cycle-life anode-free cells without excessive Li.

Considering the intrinsic electrochemical instability of LPSCl against Li, one solution is to introduce an interlayer to separate Li and LPSCl. Researchers at Samsung have developed a silver−carbon interlayer between LPSCl and stainless-steel current collectors.[30] Mitlin et al. have reported the Li_2Te interlayer for LPSCl-based anode-free batteries.[21] In both cases, ICE has been improved to over 90%. Nonetheless, LPSCl is still not intrinsically stable with alloy-based interlayers, leading to electrolyte decompositions. Therefore,

further improvement in CEs can be anticipated by preventing LPSCl decomposition.

In this work, we introduce a hydride-based interlayer, $3LiBH_4−LiI$ (LBHI), for LPSCl-based anode-free batteries. LBHI has been known for its excellent electrochemical stability at low potential.[31−33] The utilization of this interlayer resulted in a large increase in the ICE, and anode-free full cells with LBHI interlayers demonstrated improved electrochemical performance. Moreover, by monitoring the stack pressure evolution, we elucidate the failure mechanism, i.e., "soft shorting", in solid-state anode-free cells. Until now, soft shorting has remained poorly understood, primarily due to challenges in characterizing Li dendrites. These dendrites are small in size and are insensitive to X-ray and electro-based techniques. Our research emphasizes that both the formation of Li dendrites and the deformation of plated Li metal contribute to the soft shorting of solid-state anode-free batteries.

We first studied Li plating and stripping behaviors in anode-free half cells. Bare Cu served as current collectors, and $Li_{0.5}In$ (Li−In) alloy with overly excessive lithium was used as the counter and reference electrode because (i) Li−In has a smaller volume change than Li metal during charge and discharge, and (ii) its stable, relatively high electrode potential (∼0.6 V vs Li⁺/Li) helps prevent Li plating on Li−In. Previous work has also employed Li−In reference electrodes to study Li behaviors.[34] Because of the excellent kinetics of alloying/dealloying processes in Li−In, the overpotential of Li−In is very small (<0.002 V, Figure S1) at the current density used in this work, and therefore, the overpotential from Cu|Li−In half cells is mainly due to Li plating/stripping on the Cu electrode.
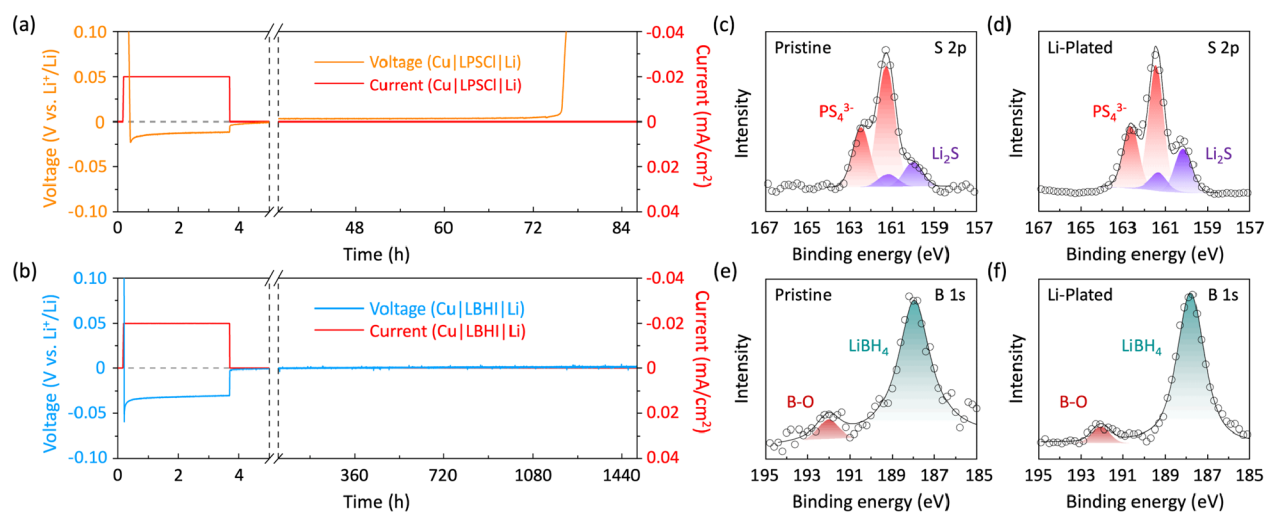
Figure 2. Voltage profiles of (a) Cu|LPSCl|Li and (b) Cu|LBHI|Li cells. In-situ Li was plated at 0.02 mA/cm² for 3.5 h, and after Li plating, open-circuit voltages were monitored to evaluate the interfacial stability between SEs and Li. The XPS spectra of (c, d) S 2p and (e, f) B 1s of LPSCl and LBHI before and after Li plating, respectively.

These half cells were discharged at 0.05 mA/cm² for 4 h during which Li was plated on Cu, followed by charging back to ~0.4 V vs Li−In (1.0 V vs Li⁺/Li) for Li stripping. A small areal capacity was used for the Li plating/stripping experiment to prevent dendrite formation during the study of electrochemical stability of the interlayer.

Figure 1(a) shows the voltage profiles of the Cu|LPSCl|Li−In half cell for the first two cycles. A voltage slope is observed at the initial part of Li plating, corresponding to LPSCl decomposition. The 70.3% ICE indicates a large irreversibility for Li cycling. Even in the second cycle, the CE remains low at 73.2%. It should be noted that a higher ICE (77.3%) can be achieved by replacing LPSCl with a Li_3PS_4 (LPS) glass electrolyte (Figure S2). These ICE values are consistent with previously reported ICEs of sulfide-based anode-free half cells (~80%), albeit slightly lower due to different experimental conditions. Moreover, these ICEs are lower than those typically reported in liquid-electrolyte anode-free batteries, highlighting the challenges of using sulfide-based SEs in anode-free batteries. Figure 1(b) displays the voltage profiles of anode-free half cell with LBHI interlayer. 12 mg of LBHI was cold-pressed onto LPSCl, resulting in an interlayer thickness of ~100 μm. The ICE for Cu|LBHI|LPSCl|Li−In is 94.7% and then increases to 95.5% for the second cycle, suggesting that the integration of the LBHI interlayer effectively improves the reversibility of Li cycling. One interesting finding is that applying 15 MPa stack pressure can reduce ICEs (Figure S3), and this might be caused by incomplete Li stripping due to the extrusion of plated Li into the surface porosities of SEs. The morphology of the plated Li shows distinct features with a disperse, spherical shape for the cell without the LBHI interlayer (Figure S4) and a fiber-like dense Li with the interlayer (Figures S5 and S6). The large amount of residual Li on the LPSCl solid electrolyte side (Figure S4) after peeling off Cu implies strong reactions between LPSCl and the plated Li.

To further study the LBHI interlayer, we conducted impedance measurements in Cu|LPSCl|Li−In (Figure 1(c) and (d)) and Cu|LBHI|LPSCl|Li−In (Figure 1(e) and (f)) half cells during the first cycle. In both cases, the prolonged straight tail at low frequencies gradually diminishes during Li plating, corresponding to the transition from blocking to nonblocking

electrode as Li plates on Cu. The reappearance of the tail after charging Cu|SE|Li−In cells to 1.0 V vs Li⁺/Li indicates a return to the blocking configuration after Li stripping. Based on the Nyquist plots of Li−In|LPSCl|Li−In and Li|LPSCl|Li (Figure S4(a) and (b)), the characteristic frequency for the LPSCl resistance is before 32 kHz. Therefore, in Figure 1(c) and (d), the semicircles at 700−32 and 32−1.5 kHz are attributed to the resistances of LPSCl and SEI, respectively. While the 1.5 kHz−2 Hz semicircle represents the interfacial charge-transfer resistance. These assignments on semicircles align well with previous reports.[26,35] For more details, please refer to the Supporting Information. Figure S5(a) and (b) show that SEI resistance remains consistently small and stable, although we anticipate it will increase after multiple cycles.[27] Notably, a clear change in interfacial resistance, decreasing during Li plating but increasing during Li stripping, has been observed due to variations in the amount of plated Li.

From the Nyquist plots of Li|LBHI|LPSCl|LBHI|Li (Figure S7(c)), the characteristic frequencies for the SE resistance and the interfacial charge-transfer resistance are 220 kHz−32 kHz and 32 kHz−15 Hz, respectively. Therefore, in Figure 1(e) and (f), the Nyquist plots of Cu|LBHI|LPSCl|Li−In can be divided into two regions: a high-frequency semicircle before 32 kHz representing the resistances of LPSCl and LBHI, and a low-frequency semicircle (32 kHz−0.7 kHz) corresponding to the interfacial charge-transfer resistance. There is no observable SEI resistance in Cu|LBHI|LPSCl|Li−In. Compared to Cu|LPSCl|Li−In (Figure S8(a) and (b)), Cu|LBHI|LPSCl|Li−In (Figure S8(c) and (d)) exhibits higher SE resistance due to the lower ionic conductivity of LBHI, and we also observe a similar changing trend in interfacial resistance as in Cu|LPSCl|Li−In. Overall, despite the relatively high SE and interfacial resistances, no semicircle corresponding to interphase formation can be observed for the cell with the LBHI interlayer.

It has been reported that the interfacial stability between SEs and Li strongly correlates with the surface chemistry and microstructure of Li.[27,36,37] To assess the (electro)chemical stability between SEs and in situ formed Li, we monitored the evolution of open-circuit voltage (OCV) in Cu|LPSCl|Li and Cu|LBHI|Li cells after plating Li at 0.02 mA/cm² for 3.5 h
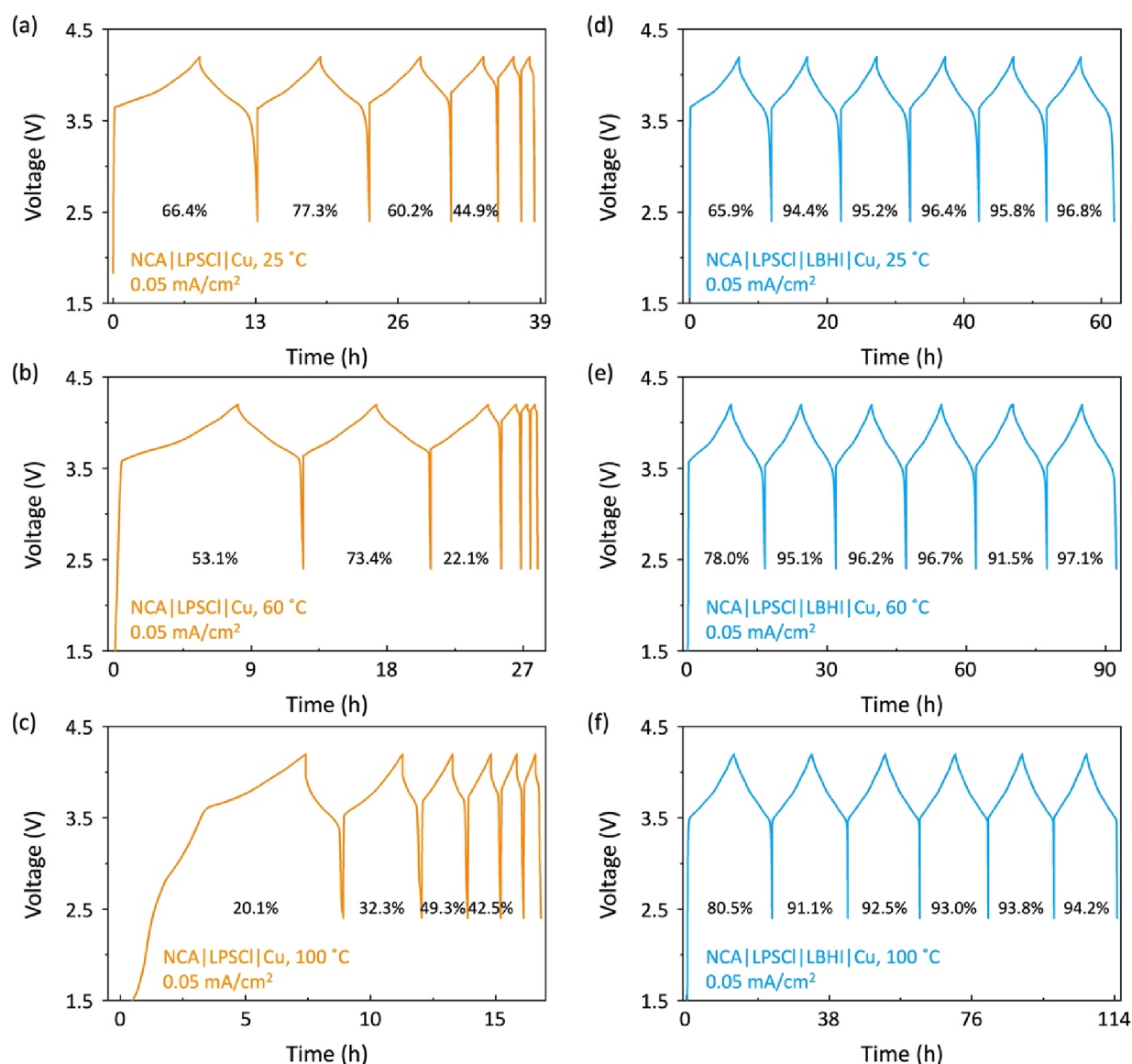
Figure 3. Voltage profiles of (a–c) NCA|LPSCl|Cu and (d–f) NCA|LPSCl|LBHI|Cu full cells. The full cells were tested at 0.05 mA/cm² within a voltage range of 2.4–4.2 V at (a, d) 25 °C, (b, e) 60 °C, and (c, f) 100 °C under a stack pressure of 15 MPa. Percentage values represent the CE for each cycle.

(equivalent to ∼0.35 μm thick of Li). In Cu|LPSCl|Li (Figure 2(a)), a sharp increase in the level of the OCV becomes evident after about 3 days of storage, indicating Li/LPSCl side reactions and the formation of interphases with higher potentials than pure Li. While the OCV of Cu|LBHI|Li remains stable at 0 V vs Li⁺/Li even after 60 days (Figure 2(b)). The superior (electro)chemical stability of LBHI is also supported by the much smaller currents observed during the Linear Sweep Voltammetry (LSV) (Figure S9). Furthermore, the mechanism for the greater nucleation overpotential in Cu|LBHI|Li (Figure 2(b)) than in Cu|LPSCl|Li (Figure 2(a)) is proposed in the Supporting Information.

The stabilities between SEs and the plated Li are also analyzed by XPS. As indicated by the S 2p spectra (Figure 2(c) and (d)), an increase in Li_2S intensity is due to LPSCl decomposition at low potentials. Conversely, no apparent change can be observed in the B 1s spectra after 60 days of storage, as shown in Figure 2(e) and (f). B−O signals in the B 1s spectra are possibly attributed to surface electrolyte

oxidation during the sample transfer process. These results confirm the exceptional electrochemical and chemical stabilities between LBHI and plated Li.

Figure 3 presents the electrochemical performances of NCA| LPSCl||Cu and NCA|LPSCl||LBHI|Cu using the single-crystal-line NCA cathode. These full cells were cycled at a current of 0.05 mA/cm² (∼1/8 C, based on a current of 180 mAh/g_{NCA}). The ICEs for NCA|LPSCl||Cu full cells are 66.4%, 53.1%, and 20.1% at 25 °C (Figure 3(a)), 60 °C (Figure 3(b)), and 100 °C (Figure 3(c)), respectively. However, NCA|LPSCl||LBHI| Cu full cells exhibit ICEs of 65.9% at 25 °C (Figure 3(d)), 78.0% at 60 °C (Figure 3(e)), and 80.5% at 100 °C (Figure 3(f)). Moreover, NCA|LPSCl||LBHI|Cu delivers higher specific capacities than NCA|LPSCl||Cu at each temperature (Figure S10), and CEs rise to >90% for the subsequent cycles. Therefore, solid-state anode-free full cells with the LBHI interlayer demonstrate superior electrochemical performance. This improvement in electrochemical performance is partic-ularly pronounced at high temperatures. This is because, for
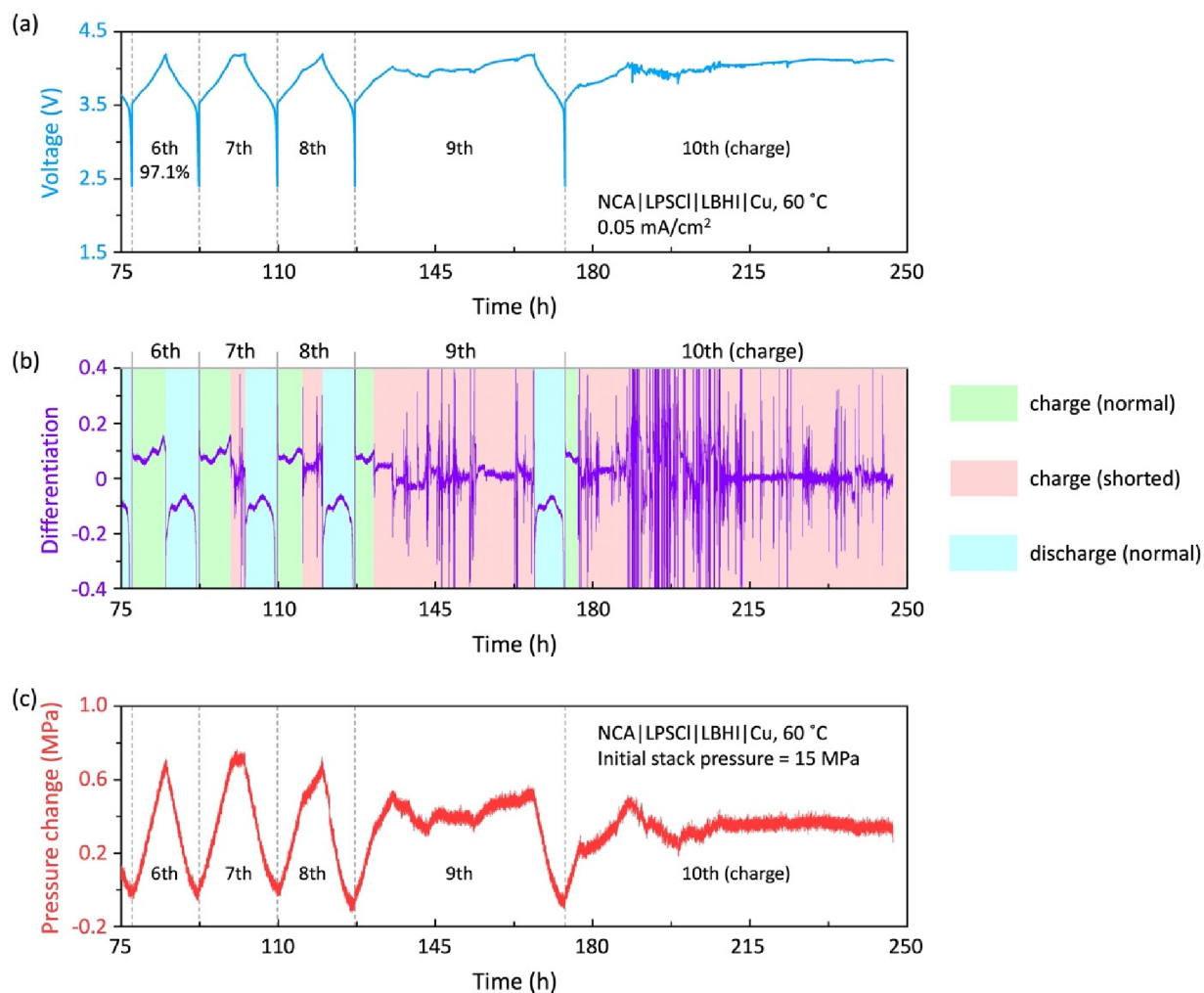
Figure 4. Evolutions of (a) voltage, (b) differential voltage, and (c) pressure change in the NCA|LPSCl|LBHI|Cu full cell (60 °C) from the sixth to the tenth cycle during the galvanostatic charge/discharge tests.
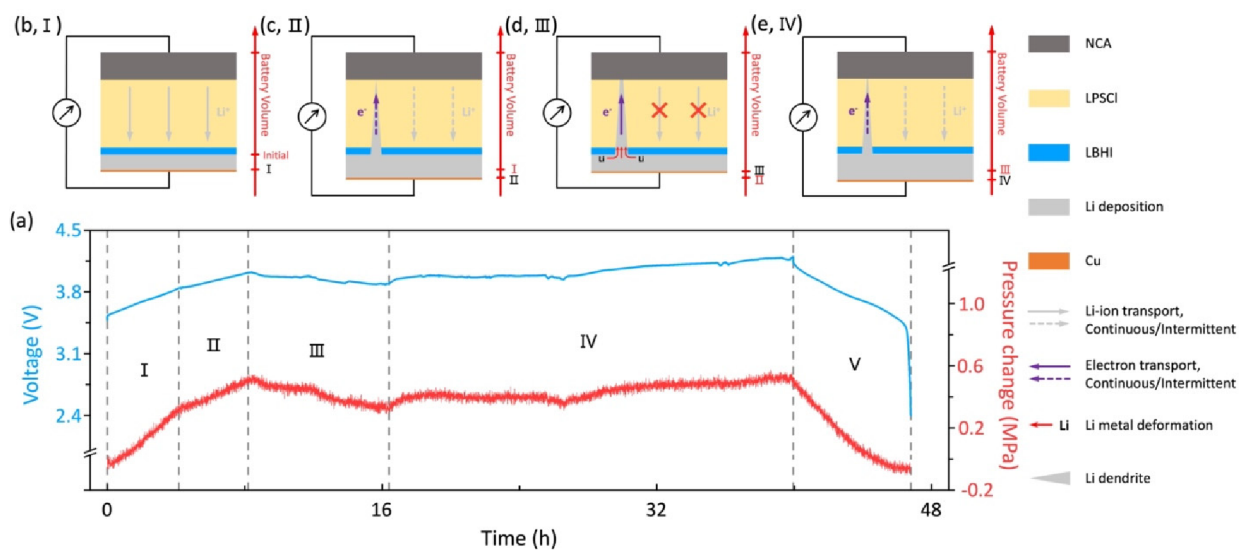

Figure 5. (a) The voltage and the corresponding pressure change profiles of NCA|LPSCl|LBHI|Cu full cell during the ninth cycle and (b-e) schematic diagrams illustrating the Stages I−IV.

LBHI with excellent cathodic stability, an increased temperature enhances its kinetics; but for unstable SEs such as LPSCl,

higher temperatures promote their side reactions with Li. These results further validate the exceptional (electro)chemical stability between Li and LBHI.

So far, we have demonstrated that the LBHI interlayer can effectively improve the electrochemical performance of solid-state anode-free batteries. However, NCA|LPSCl|LBHI|Cu cells exhibit a limited cycle life. Voltage fluctuations have been observed since the seventh cycle (Figure 4(a)), and ultimately lead to an incomplete charge process in the tenth cycle. This phenomenon is more evident in differential voltage curves (Figure 4(b)). Notably, there are no abnormal voltage profiles during discharge. This type of cell failure is not exclusive to our anode-free batteries, it has been reported in solid-state Li metal batteries,[28,38−40] commonly described as "soft shorting" or "shorting" due to Li dendrite formation. Combining semi-quantitative impedance analysis and computational modeling, Counihan et al.[41] provided a very detailed study on the dynamic behavior of soft-shorting in Li metal based symmetric and half cells with polymer-ceramic composite electrolyte and highlights possible mechanisms of forming, unshorting, and reshorting during soft-shorting. The detailed mechanisms of soft-shorting in an anode-free full cell with a sulfide-based solid electrolyte, to our knowledge, have not been reported. Figure 4(c) shows the stack pressure change, which is the difference between the measured stack pressure of the cell during charge−discharge and the initial stack pressure (15 MPa), starting from the sixth cycle onward. During charge, the volume of the NCA cathode decreases while the volume on the anode side increases due to Li plating. However, for the same capacity transferred from cathode to anode, the volume change of NCA (<6%)[42] is considerably smaller than that of Li metal. Consequently, the net volume of the full cell is mainly due to the anode side; it increases during charge and decreases during discharge. Monitoring the stack pressure change can thus provide insights into Li cycling behaviors.

Interestingly, we observe a strong correlation between Figure 4(c) and (a): stack pressure increases and decreases synchronously with the cell voltage change, including the fluctuated voltage profiles, which are mirrored in the stack pressure curves. This strong correlation is consistent across other failed anode-free full cells (Figure S11). Based on the analysis of voltage and stack pressure changes, we propose that soft shorting is attributed to both the formation of Li dendrites and the deformation of plated bulk Li. We use the ninth cycle as an example to illustrate this mechanism, as shown in Figure 5.

In the initial charge period, Li can be plated onto the Cu surface without dendrite formation, leading to a normal increase in both the cell voltage and stack pressure (Figure 5(a)). This process is termed Stage I, as shown in Figure 5(b). However, in Stage II (Figure 5(c)), the cell voltage increases but at a reduced rate, and the pressure also exhibits a synchronized trend with voltage. Stage II is featured by the formation and penetration of Li dendrites through SEs. As Li dendrites reach the NCA, charge transport in the cell shifts from ionic transport by the SE to electronic transport through the metallic Li dendrites, preventing further Li deposition. During the early appearance of Li dendrites, their content is limited. Li dendrites chemically reduce the charged NCA, lowering the cathode potential.[41] Once the dendrites are chemically reacted, the cathode potential increases again due to electrochemical charging (or oxidation) of NCA by the applied current, and SE also regains its function to transport

lithium ions until the next dendrite-NCA contact, thereby resuming Li plating and the corresponding stack pressure increase. Stage II is dominated by the electrochemical oxidization of NCA. As a result, the full cell still exhibits voltage and stack pressure increases but at a reduced rate.

Stage III (Figure 5(d)) is marked by a phenomenon that both voltage and stack pressure decrease simultaneously. This voltage decrease is dominated by the chemical reduction of NCA as Li dendrites exist. Therefore, no Li metal is electrochemically plated on Cu during Stage III because of the facilitated electron transport through Li dendrites. The decreased stack pressure means a reduction in the thickness of plated Li metal, which suggests that the plated bulk Li can deform and infiltrate into SEs, probably by utilizing pathways such as pores, cracks, and Li dendrites. This hypothesis is supported by full cells with higher stack pressures but soft-shorted in the first charge, as shown in Figure S12. Moreover, the deformation and infiltration of bulk Li can sustain Li dendrites without the necessity for electrochemical plating during Stage III. However, not all the plated Li infiltrates the SE because the pressure change does not drop to 0 MPa. The entire process may be accelerated by the melting of Li dendrites, as internal short-circuiting is known for Joule heat generation.[41,43,44]

When Li dendrites cannot be sustained by the mechanical deformation and infiltration of bulk Li, the cell voltage and stack pressure start to rise again in Stage IV (Figure 5(e)). Stage IV shares intrinsic similarities with Stage II, indicating that electrochemical oxidation of NCA dominates the full cell during Stage IV. Stage V represents the discharge process of the full cell during which both voltage and stack pressure decrease normally without dendrite formation.

This proposed mechanism, which combines chemical reduction and electrochemical oxidation of NCA with macroscopic Li deformation, is supported by the increased full-cell resistance due to the severe chemical reactions between NCA and Li dendrites after the ninth discharge (Figure S13). As shown in Figure S14, galvanotactic electro-chemical impedance spectra (GEIS) were also used to study the soft-shorting mechanism. However, no apparent change in the impedance spectra was observed during soft shorting, indicating the limitation of using GEIS to study soft shoring in SSBs. This limitation is probably due to the small amount of dendrite formation and the rapid reaction between Li dendrites and LPSCl SE, highlighting the importance of developing more advanced, in situ characterization techniques with a higher detection limit for low-content Li.[45]

Figures 4 and 5 provide valuable insights into the impacts of Li dendrite formation and Li metal deformation on voltage and stack pressure changes in solid-state anode-free batteries. We believe that this soft-shorting mechanism can be broadly extended to other solid-state Li metal batteries. However, although incorporating an LBHI interlayer can ensure highly stable interfaces, it should be noted that (electro)chemical stability is not the only consideration for high-performance anode-free batteries. In Supporting Information, we have discussed the limitations of LBHI despite its excellent stabilities with Li metal. Figure S15 compares the nucleation overpotentials of SEs under different conditions. Figures S16 and S17 show the morphologies of in situ-plated Li from optical, SEM, and neutron images. Residual Li can be observed after Li stripping, suggesting that incomplete stripping is one important reason for less than 100% ICE. We suggest that

combining LBHI interlayers with other interlayers, such as Ag–C[30] and Li$_2$Te,[21] could be favorable in guiding dense and homogeneous Li deposition. However, additional challenges may arise in the complicated manufacturing of multi-interlayer SSBs. The remarkable stability of LBHI with Li implies its potential use as an ideal ionic conductor for three-dimensional anodes.[31,46] Additional implications include the development of predictive diagnostic tools for monitoring the safety of SSBs, as the pressure evolution can offer important information about battery failure. It should also be noted that, due to the fabrication method by spraying powers, the LBHI interlayer in the present work is quite thick. Further study will be needed to reduce its thickness to <10 μm for its practical application. The excellent stability of hydrides in some solvents such as tetrahydrofuran[47] and the low melting point of LBHI[48] provide opportunities to develop liquid-based approach to apply a thinner interlayer.

In summary, we reported the utilization of LBHI as an interlayer in anode-free batteries. This hydride-based interlayer has demonstrated excellent chemical and electrochemical stabilities with in situ plated Li. A significant improvement in ICE can be observed in anode-free half cells with the LBHI interlayer. The superior interfacial stability between LBHI and Li also enabled anode-free full cells with improvements in both CEs and specific capacities. By monitoring the stack pressure evolution, we observed a direct correlation between the voltage and pressure change during soft shorting. A mechanism was proposed to explain this soft-shorting behavior based on Li dendrite formation and the plastic deformation of plated Li. These findings highlight the importance of managing mechanical deformation to suppress Li dendrites and provide crucial insights into understanding the soft-shorting mechanism for the future development of solid-state Li metal batteries.

ASSOCIATED CONTENT

Supporting Information

The Supporting Information is available free of charge at https://pubs.acs.org/doi/10.1021/acsenergylett.4c00704.

Synthesis of electrode and electrolyte materials; procedures of cell fabrication, electrochemical test, material characterization, and stack pressure measurement; voltage profiles of Li–In|LPSCl|Li–In cell, voltage profiles and ICE of the Cu|LPS|LPSCl|Li–In half cell, first-cycle voltage profiles and ICEs of Cu|LBHI|LPSCl| Li–In, Cu|LPSCl|Li–In, and Cu|LPS|LPSCl|Li–In half cells, Nyquist plots of Li–In|LPSCl|Li–In, Li|LPSCl|Li, and Li|LBHI|LPSCl|LBHI|Li, Nyquist plots of half cells after 4 h Li plating and the summary of fitting results, LSV curves, specific capacities of NCA|LPSCl|LBHI|Cu and NCA|LPSCl|Cu full cells, the repeated experiment of NCA|LPSCl|LBHI|Cu full cell, the initial charge curves of NCA|LPSCl|LBHI|Cu full cells with various stack pressure, Nyquist plots of NCA|LPSCl|Cu full cell, the application of GEIS in monitoring Li dendrites; discussions on the greater nucleation overpotential in Cu|LBHI|Li cell than in Cu|LPSCl|Li cell; discussions on the limitations of the LBHI interlayer (PDF)

AUTHOR INFORMATION

Corresponding Author

Fudong Han − *Department of Mechanical, Aerospace and Nuclear Engineering, Rensselaer Polytechnic Institute, Troy, New York 12180, United States;* ⓘ orcid.org/0000-0003-2507-4340; Email: hanf2@rpi.edu

Authors

Yonglin Huang − *Department of Mechanical, Aerospace and Nuclear Engineering, Rensselaer Polytechnic Institute, Troy, New York 12180, United States*

Yuxuan Zhang − *Neutron Scattering Division, Oak Ridge National Laboratory, Oak Ridge, Tennessee 37830, United States;* ⓘ orcid.org/0000-0002-0083-1408

Ruixin Wu − *Department of Mechanical, Aerospace and Nuclear Engineering, Rensselaer Polytechnic Institute, Troy, New York 12180, United States*

Bowen Shao − *Department of Mechanical, Aerospace and Nuclear Engineering, Rensselaer Polytechnic Institute, Troy, New York 12180, United States*

Ruihao Deng − *Department of Mechanical, Aerospace and Nuclear Engineering, Rensselaer Polytechnic Institute, Troy, New York 12180, United States*

Ratnottam Das − *Department of Mechanical, Aerospace and Nuclear Engineering, Rensselaer Polytechnic Institute, Troy, New York 12180, United States*

Complete contact information is available at:
https://pubs.acs.org/10.1021/acsenergylett.4c00704

Author Contributions

Y. Huang contributed to the experiments, data analysis, figure making, and manuscript writing. Y. Zhang contributed to the neutron imaging and analysis. All authors discussed the results. F. Han conceived the idea and supervised the project.

Notes

The authors declare no competing financial interest.

REFERENCES

(1) Weber, R.; Genovese, M.; Louli, A.; Hames, S.; Martin, C.; Hill, I. G.; Dahn, J. Long cycle life and dendrite-free lithium morphology in anode-free lithium pouch cells enabled by a dual-salt liquid electrolyte. *Nature Energy* **2019**, *4* (8), 683−689.

(2) Eldesoky, A.; Louli, A.; Benson, A.; Dahn, J. Cycling performance of NMC811 anode-free pouch cells with 65 different electrolyte formulations. *J. Electrochem. Soc.* **2021**, *168* (12), No. 120508.

(3) Pande, V.; Viswanathan, V. Computational screening of current collectors for enabling anode-free lithium metal batteries. *ACS Energy Letters* **2019**, *4* (12), 2952−2959.

(4) Kwon, H.; Lee, J.-H.; Roh, Y.; Baek, J.; Shin, D. J.; Yoon, J. K.; Ha, H. J.; Kim, J. Y.; Kim, H.-T. An electron-deficient carbon current collector for anode-free Li-metal batteries. *Nat. Commun.* **2021**, *12* (1), 5537.

(5) Qian, J.; Adams, B. D.; Zheng, J.; Xu, W.; Henderson, W. A.; Wang, J.; Bowden, M. E.; Xu, S.; Hu, J.; Zhang, J. G. Anode-free rechargeable lithium metal batteries. *Adv. Funct. Mater.* **2016**, *26* (39), 7094−7102.

(6) Heubner, C.; Maletti, S.; Auer, H.; Hüttl, J.; Voigt, K.; Lohrberg, O.; Nikolowski, K.; Partsch, M.; Michaelis, A. From lithium-metal toward anode-free solid-state batteries: Current developments, issues, and challenges. *Adv. Funct. Mater.* **2021**, *31* (51), No. 2106608.

(7) Xu, R.; Cheng, X.-B.; Yan, C.; Zhang, X.-Q.; Xiao, Y.; Zhao, C.-Z.; Huang, J.-Q.; Zhang, Q. Artificial interphases for highly stable lithium metal anode. *Matter* **2019**, *1* (2), 317−344.

(8) Huang, Y.; Shao, B.; Han, F. Solid-state batteries: an introduction. In *Solid State Batteries Vol. 1: Emerging Materials and Applications*; Gupta, R. K., Ed.; ACS Publications: 2022; pp 1−20.

(9) Bates, J.; Dudney, N.; Gruzalski, G.; Zuhr, R.; Choudhury, A.; Luck, C.; Robertson, J. Fabrication and characterization of amorphous lithium electrolyte thin films and rechargeable thin-film batteries. *J. Power Sources* **1993**, *43* (1−3), 103−110.

(10) Neudecker, B.; Dudney, N.; Bates, J. Lithium-free" thin-film battery with in situ plated Li anode. *J. Electrochem. Soc.* **2000**, *147* (2), 517.

(11) Wang, M. J.; Carmona, E.; Gupta, A.; Albertus, P.; Sakamoto, J. Enabling "lithium-free" manufacturing of pure lithium metal solid-state batteries through in situ plating. *Nat. Commun.* **2020**, *11* (1), 1−9.

(12) Kazyak, E.; Wang, M. J.; Lee, K.; Yadavalli, S.; Sanchez, A. J.; Thouless, M.; Sakamoto, J.; Dasgupta, N. P. Understanding the electro-chemo-mechanics of Li plating in anode-free solid-state batteries with operando 3D microscopy. *Matter* **2022**, *5* (11), 3912−3934.

(13) Lee, K.; Kazyak, E.; Wang, M. J.; Dasgupta, N. P.; Sakamoto, J. Analyzing void formation and rewetting of thin in situ-formed Li anodes on LLZO. *Joule* **2022**, *6* (11), 2547−2565.

(14) Yi, E.; Wang, W.; Kieffer, J.; Laine, R. M. Flame made nanoparticles permit processing of dense, flexible, Li+ conducting ceramic electrolyte thin films of cubic-Li7La3Zr2O 12 (c-LLZO). *Journal of Materials Chemistry A* **2016**, *4* (33), 12947−12954.

(15) Miara, L. J.; Richards, W. D.; Wang, Y. E.; Ceder, G. First-principles studies on cation dopants and electrolyte| cathode interphases for lithium garnets. *Chem. Mater.* **2015**, *27* (11), 4040−4047.

(16) Kim, K. J.; Rupp, J. L. All ceramic cathode composite design and manufacturing towards low interfacial resistance for garnet-based solid-state lithium batteries. *Energy Environ. Sci.* **2020**, *13* (12), 4930−4945.

(17) Yue, J.; Huang, Y.; Liu, S.; Chen, J.; Han, F.; Wang, C. Rational designed mixed-conductive sulfur cathodes for all-solid-state lithium batteries. *ACS Appl. Mater. Interfaces* **2020**, *12* (32), 36066−36071.

(18) Fan, X.; Ji, X.; Han, F.; Yue, J.; Chen, J.; Chen, L.; Deng, T.; Jiang, J.; Wang, C. Fluorinated solid electrolyte interphase enables highly reversible solid-state Li metal battery. *Science Advances* **2018**, *4* (12), No. eaau9245.

(19) Davis, A. L.; Kazyak, E.; Liao, D. W.; Wood, K. N.; Dasgupta, N. P. Operando analysis of interphase dynamics in anode-free solid-state batteries with sulfide electrolytes. *J. Electrochem. Soc.* **2021**, *168* (7), No. 070557.

(20) Lewis, J. A.; Sandoval, S. E.; Liu, Y.; Nelson, D. L.; Yoon, S. G.; Wang, R.; Zhao, Y.; Tian, M.; Shevchenko, P.; Martinez-Paneda, E.; McDowell, M. T. Accelerated short circuiting in anode-free solid-state batteries driven by local lithium depletion. *Adv. Energy Mater.* **2023**, *13* (12), No. 2204186.

(21) Wang, Y.; Liu, Y.; Nguyen, M.; Cho, J.; Katyal, N.; Vishnugopi, B. S.; Hao, H.; Fang, R.; Wu, N.; Liu, P.; et al. Stable anode-free all-solid-state lithium battery through tuned metal wetting on the copper current collector. *Adv. Mater.* **2023**, *35*, No. 2206762.

(22) Banerjee, A.; Tang, H.; Wang, X.; Cheng, J.-H.; Nguyen, H.; Zhang, M.; Tan, D. H.; Wynn, T. A.; Wu, E. A.; Doux, J.-M.; et al. Revealing nanoscale solid−solid interfacial phenomena for long-life

and high-energy all-solid-state batteries. *ACS Appl. Mater. Interfaces* **2019**, *11* (46), 43138−43145.

(23) Zhu, Y.; He, X.; Mo, Y. Origin of outstanding stability in the lithium solid electrolyte materials: insights from thermodynamic analyses based on first-principles calculations. *ACS Appl. Mater. Interfaces* **2015**, *7* (42), 23685−23693.

(24) Schwietert, T. K.; Arszelewska, V. A.; Wang, C.; Yu, C.; Vasileiadis, A.; de Klerk, N. J.; Hageman, J.; Hupfer, T.; Kerkamm, I.; Xu, Y.; et al. Clarifying the relationship between redox activity and electrochemical stability in solid electrolytes. *Nat. Mater.* **2020**, *19* (4), 428−435.

(25) Otto, S. K.; Riegger, L. M.; Fuchs, T.; Kayser, S.; Schweitzer, P.; Burkhardt, S.; Henss, A.; Janek, J. In situ investigation of lithium metal−solid electrolyte anode interfaces with ToF-SIMS. *Advanced Materials Interfaces* **2022**, *9* (13), No. 2102387.

(26) Wenzel, S.; Sedlmaier, S. J.; Dietrich, C.; Zeier, W. G.; Janek, J. Interfacial reactivity and interphase growth of argyrodite solid electrolytes at lithium metal electrodes. *Solid State Ionics* **2018**, *318*, 102−112.

(27) Riegger, L. M.; Mittelsdorf, S.; Fuchs, T.; Rueß, R.; Richter, F. H.; Janek, J. r. Evolution of the interphase between argyrodite-based solid electrolytes and the lithium metal anode—The kinetics of solid electrolyte interphase growth. *Chem. Mater.* **2023**, *35*, 5091−5099.

(28) Lewis, J. A.; Lee, C.; Liu, Y.; Han, S. Y.; Prakash, D.; Klein, E. J.; Lee, H.-W.; McDowell, M. T. Role of areal capacity in determining short circuiting of sulfide-based solid-state batteries. *ACS Appl. Mater. Interfaces* **2022**, *14* (3), 4051−4060.

(29) Zou, C.; Yang, L.; Luo, K.; Liu, L.; Tao, X.; Yi, L.; Liu, X.; Zhang, X.; Wang, X. In situ formed protective layer: toward a more stable interface between the lithium metal anode and Li6PS5Cl solid electrolyte. *ACS Applied Energy Materials* **2022**, *5* (7), 8428−8436.

(30) Lee, Y.-G.; Fujiki, S.; Jung, C.; Suzuki, N.; Yashiro, N.; Omoda, R.; Ko, D.-S.; Shiratsuchi, T.; Sugimoto, T.; Ryu, S.; et al. High-energy long-cycling all-solid-state lithium metal batteries enabled by silver−carbon composite anodes. *Nature Energy* **2020**, *5* (4), 299−308.

(31) Huang, Y.; Shao, B.; Wang, Y.; Han, F. Solid-state silicon anode with extremely high initial coulombic efficiency. *Energy Environ. Sci.* **2023**, *16* (4), 1569−1580.

(32) Sveinbjörnsson, D.; Christiansen, A. S.; Viskinde, R.; Norby, P.; Vegge, T. The LiBH4-LiI solid solution as an electrolyte in an all-solid-state battery. *J. Electrochem. Soc.* **2014**, *161* (9), A1432.

(33) Kisu, K.; Kim, S.; Oguchi, H.; Toyama, N.; Orimo, S.-i. Interfacial stability between LiBH4-based complex hydride solid electrolytes and Li metal anode for all-solid-state Li batteries. *J. Power Sources* **2019**, *436*, No. 226821.

(34) Wang, Y.; Liu, T.; Kumar, J. Effect of pressure on lithium metal deposition and stripping against sulfide-based solid electrolytes. *ACS Appl. Mater. Interfaces* **2020**, *12* (31), 34771−34776.

(35) Wenzel, S.; Weber, D. A.; Leichtweiss, T.; Busche, M. R.; Sann, J.; Janek, J. Interphase formation and degradation of charge transfer kinetics between a lithium metal anode and highly crystalline Li7P3S11 solid electrolyte. *Solid State Ionics* **2016**, *286*, 24−33.

(36) Sandoval, S. E.; McDowell, M. T. Lithium metal anodes in solid-state batteries: Metal microstructure matters. *Matter* **2023**, *6* (7), 2101−2102.

(37) Huang, Y.; Shao, B.; Han, F. Interfacial challenges in all-solid-state lithium batteries. *Current Opinion in Electrochemistry* **2022**, *33*, No. 100933.

(38) Huang, Y.; Shao, B.; Han, F. Li alloy anodes for high-rate and high-areal-capacity solid-state batteries. *Journal of Materials Chemistry A* **2022**, *10* (23), 12350−12358.

(39) Sahore, R.; Yang, G.; Chen, X. C.; Tsai, W.-Y.; Li, J.; Dudney, N. J.; Westover, A. A bilayer electrolyte design to enable high-areal-capacity composite cathodes in polymer electrolytes based solid-state lithium metal batteries. *ACS Applied Energy Materials* **2022**, *5* (2), 1409−1413.

(40) Reisecker, V.; Flatscher, F.; Porz, L.; Fincher, C.; Todt, J.; Hanghofer, I.; Hennige, V.; Linares-Moreau, M.; Falcaro, P.; Ganschow, S.; et al. Effect of pulse-current-based protocols on the

lithium dendrite formation and evolution in all-solid-state batteries. *Nat. Commun.* **2023**, *14* (1), 2432.

(41) Counihan, M. J.; Chavan, K. S.; Barai, P.; Powers, D. J.; Zhang, Y.; Srinivasan, V.; Tepavcevic, S. The phantom menace of dynamic soft-shorts in solid-state battery research. *Joule* **2024**, *8* (1), 64−90.

(42) Koerver, R.; Zhang, W.; de Biasi, L.; Schweidler, S.; Kondrakov, A. O.; Kolling, S.; Brezesinski, T.; Hartmann, P.; Zeier, W. G.; Janek, J. Chemo-mechanical expansion of lithium electrode materials−on the route to mechanically optimized all-solid-state batteries. *Energy Environ. Sci.* **2018**, *11* (8), 2142−2158.

(43) Feng, X.; Ouyang, M.; Liu, X.; Lu, L.; Xia, Y.; He, X. Thermal runaway mechanism of lithium ion battery for electric vehicles: A review. *Energy storage materials* **2018**, *10*, 246−267.

(44) Feng, X.; He, X.; Ouyang, M.; Wang, L.; Lu, L.; Ren, D.; Santhanagopalan, S. A coupled electrochemical-thermal failure model for predicting the thermal runaway behavior of lithium-ion batteries. *J. Electrochem. Soc.* **2018**, *165* (16), A3748.

(45) Dixit, M. B.; Vishugopi, B. S.; Zaman, W.; Kenesei, P.; Park, J.-S.; Almer, J.; Mukherjee, P. P.; Hatzell, K. B. Polymorphism of garnet solid electrolytes and its implications for grain-level chemo-mechanics. *Nat. Mater.* **2022**, *21* (11), 1298−1305.

(46) Mo, F.; Chi, X.; Yang, S.; Wu, F.; Song, Y.; Sun, D.; Yao, Y.; Fang, F. Stable three-dimensional metal hydride anodes for solid-state lithium storage. *Energy Storage Materials* **2019**, *18*, 423−428.

(47) Kuwata, H.; Matsui, M.; Sonoki, H.; Manabe, Y.; Imanishi, N.; Mizuhata, M. Improved cycling perforamnce of intermetallic anode by minimized SEI layer formation. *J. Electrochem. Soc.* **2018**, *165*, A1486.

(48) Lu, F.; Pang, Y.; Zhu, M.; Han, F.; Yang, J.; Fang, F.; Sun, D.; Zheng, S.; Wang, C. A high-performance Li-B-H electrolyte for all-solid-state Li batteries. *Adv. Funct. Mater.* **2019**, *29*, No. 1809219.